IEEE Access
Multidisciplinary ⋮ Rapid Review ⋮ Open Access Journal

Date of publication xxxx 00, 0000, date of current version xxxx 00, 0000.

*Digital Object Identifier 10.1109/ACCESS.2017.Doi Number*

# Design of an Interleaved Boost Serial Resonant Converter with High Transformation Ratio for Fuel Cell Battery

**Sen-Tung Wu[1], Jun-Teng Hong [1], and Ching-Chun Chuang[2]**

[1] Innovative Energy Lab. Department of Electrical Engineering, National Formosa University, Yunlin county 632301, Taiwan

[2] Department of Electrical Engineering, National Kaohsiung University of Science and Technology, Kaohsiung City 807618, Taiwan

Corresponding author: Ching-Chun Chuang (e-mail: chuang@nkust.edu.tw)

**ABSTRACT** In this study, an interleaved boost serial resonant converter with a high transformation ratio is proposed. The main architecture of this converter is a boost converter serial resonant converter, the first stage utilizes an interleaved boost converter to reduce input current ripple, In the second stage, a resonant converter is used, where power MOSFETs and rectifier diodes enable soft switching at an appropriate operating frequency. This feature improves efficiency by reducing losses caused by the hard switching of traditional circuits. Finally, this converter is designed with the rated power of 1.5kW and the digital signal processor TMS320F28335 is employed as the main system controller core to realize the wide output voltage range 40~125V from fuel cell as an input power source which can output a 400V for output load or DC bus applications through the proposed converter. The experimental results show that the maximum conversion efficiency of this converter when operating at the low input voltage 40V is up to 92.69%, and at the high input voltage 125V is up to 93.57%.

**INDEX TERMS** High transformation ratio, interleaved boost, resonant converter, soft switching, current ripple.

## I. INTRODUCTION

With economic development and technological progress, today's society has increasingly higher requirements for environmental protection and energy conservation. Traditional fossil fuels such as oil, natural gas, and coal not only continue to deplete in storage but also cause significant pollution to the environment. The development of renewable energy provides hope and receives considerable attention. Renewable energy sources include solar energy, wind power, geothermal energy, hydrogen energy, etc. Among these, solar energy and wind energy are more limited by the natural environment, while hydrogen energy shows promising potential in the field of renewable energy. Countries worldwide are gradually transitioning from fuel-powered vehicles to electric vehicles. However, due to the current limited adoption of pure electric systems, many manufacturers have turned to fuel cells as an alternative solution to meet different power requirements [1-3].As shown in Fig. 1 , a fuel cell is an electrochemical device that converts the chemical energy in the fuel into electrical energy by redox reaction through an oxidant. The fuel is mostly hydrogen or hydrocarbons that can decompose hydrogen. The advantages of low pollution, high conversion efficiency, low noise, fast startup and high current output capability have become the goals of scientific and technological development in recent years. Even though the fuel cell has many of the above advantages, unlike the general storage battery, the fuel cell itself has no storage capacity, and the output voltage range will be affected by the size of the output load, resulting in a wide range of output voltage characteristics, and there are many fuel cells. For low voltage output, it is not suitable to directly provide general load use. In order to provide a stable voltage for the load, a set of DC-DC converters are required to supply the energy to DC load. As depicted in Fig. 1, a fuel cell is an electrochemical device that utilizes a redox reaction with an oxidant to convert the chemical energy in fuel, such as hydrogen or hydrogen-decomposable hydrocarbons into electrical energy. In recent years, fuel cells have gained significant attention in scientific and technological development due to their advantages, including low pollution, high conversion efficiency, low noise, fast startup, and high current output capability. However, unlike conventional storage batteries, fuel cells do not possess inherent storage capacity. Furthermore, the output voltage range of a fuel cell is influenced by the rated power of the output load, resulting in wide-ranging voltage characteristics.

Moreover, numerous fuel cells have a low voltage output, making them unsuitable for direct use with general loads. Hence, to supply a stable voltage to the load, a DC-DC converter is required for providing DC power.

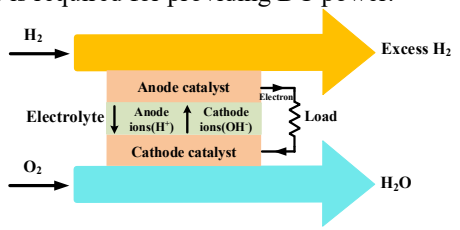


**FIGURE 1. Concept of the electrochemical reaction of a hydrogen fuel cell.**

The traditional dual-active bridge (DAB) converter is characterized by its simple architecture, ease of control, and high efficiency, featuring zero voltage switching (ZVS) and bidirectional power transfer capabilities. The control of the converter is achieved by adjusting the phase shift modulation between the two full bridges or different arms of the same bridge, allowing for output voltage regulation and power flow direction switching. The control methods can be categorized into traditional phase shift (TPS), Single Phase Shift (SPS), Dual Phase Shift (DPS), and Extended Phase Shift (EPS). In [4], [5], a detailed analysis shows that under the same power transmission conditions, the switching stress and peak inductor current of DPS control are lower than those of SPS control. The advantages of EPS over traditional phase shift control are analyzed in [6], [7], indicating that EPS can expand the adjustment range of transmitted power, reduce current stress in the circuit, decrease the circuit's backflow power, and enhance overall efficiency. In [8], to minimize the backflow power of the DAB, a control method employing DPS was compared with TPS. It was found that DPS achieves higher efficiency due to lower backflow power and offers greater flexibility in power regulation due to its larger power adjustment range. In [9], a feedback system suitable for the DAB converter was designed using a small signal model, and a PI compensator was employed to improve the feedback performance and enhance the output voltage stability.

Due to its diverse control methods, the application of the dual-active bridge (DAB) converter is also quite varied. For instance, in [10], a DAB-based converter was designed as two types of converters: a two-port and a three-port converter, both of which possess bidirectional transfer capabilities. in [11], compares various control strategies for the dual-active bridge (DAB) isolated bidirectional DC–DC converter (IBDC) and analyzes different types of control methods, including Single Phase Shift (SPS), Dual Phase Shift (DPS), Extended Phase Shift (EPS), and Traditional Phase Shift (TPS), while integrating the advantages and disadvantages of each control method. Despite the many advantages of the DAB, such as power transfer through additional inductors or the inherent leakage inductance of transformers, phase shifts exist between the primary and secondary side transformer voltages under single-phase shift control. This phase shift leads to circulating currents due to the phase difference between the transformer current and voltage, requiring the converter to supply additional energy during power transmission. Thus, the switches must endure greater current stress. Furthermore, in light-load conditions, single-phase operation results in smaller circulating currents, making it challenging to achieve soft switching, leading to a reduced range for soft switching during light loads, ultimately resulting in lower efficiency. To apply the DAB in wide input and output scenarios, challenges must be overcome, such as the inductor currents in hard-switching designs being square or triangular waves. These include high-frequency components that contribute to power switching losses and EMI noise interference, complicating both the hardware and control strategies of the circuit. A novel interleaved boost converter is proposed in [12], combining two groups of boost converters with identical duty cycles for the power switches but with driving signals that are 180 degrees out of phase. The advantages of this new interleaved boost converter include lower input current ripple and relatively higher output power.

The resonant converter itself has the characteristics of soft switching, which is beneficial to reduce the loss when the power switch is switched. Resonant converters are basically composed of inductors and capacitors. Currently, there are common LC series resonance, LLC series-parallel resonance[13], and LCC series-parallel resonance[14]. Among them, LLC resonant converters are one of the most widely used topologies.

The LLC resonant converter is a resonant circuit formed by connecting the transformer magnetizing inductance, resonant capacitor and resonant inductance in series. The converter has excellent flexible switching characteristics and can adjust the frequency without adding any auxiliary circuit. The characteristics of zero-voltage switching of the side switch and zero-current switching of the secondary side switch can greatly improve the power and efficiency of the converter. Even if the resonant converter can improve the voltage gain through the transformer and the resonant tank, even if the resonant converter has the function of voltage regulation, it cannot cope with such a wide range of current fuel cell voltage limitations.

In [15], design guidelines for LLC resonant converters are proposed, which involve designing the inductance ratio based on the required voltage gain and power factor of the circuit. This design approach effectively enhances the power factor and efficiency of the converter. Additionally, selecting appropriate magnetizing inductance and optimizing the Q factor and Ln through the gain curve can further improve the efficiency of the converter [16]. In [17], a modified PWM-LLC is proposed to meet the demand for a wide charging voltage range in on-board chargers for plug-in electric vehicles (PEVs). This approach utilizes the adjustment of the duty cycle of the secondary-side MOSFETs at a fixed output frequency to achieve a wide output voltage range. When compared to traditional control methods for LLC converters,

the PWM-LLC demonstrates higher efficiency. In [18], the use of SiC MOSFETs in LLC topology is investigated, with performance studies conducted over a frequency range from 500 kHz to 1 MHz. Experimental results indicate that SiC MOSFETs offer higher conversion efficiency compared to traditional silicon-based MOSFETs. A novel full-bridge LLC resonant converter is introduced in [19], which employs SPWM technology on the secondary side, enabling the converter to determine whether to output AC or DC voltage based on varying load conditions. This functionality allows an LLC converter, typically limited to DC loads, to also be applicable for AC loads.

The current-fed full-bridge converter [20], [21] adds an inductor in series at the input of the conventional full-bridge circuit. This inductor acts similarly to a boost inductor, allowing for a reduction in the transformer turns ratio and consequently decreasing the leakage inductance produced by the transformer. Since the duty cycle of the power switches in the circuit must exceed 50%, an overlap time occurs when all four power switches are conducting simultaneously. This overlap time is primarily intended to allow the input inductor to store energy while establishing a short circuit on the primary side of the transformer without transferring energy. With a fixed transformer turns ratio, the input voltage becomes constrained, meaning that under excessively wide input voltage conditions, the duty cycle of the switches approaches full conduction. This situation leads to the converter operating under unsafe conditions, increasing the potential for damage to the circuit components.

In [22], [23], a charger for Plug-in Electric Vehicles (PEVs) was designed, employing an LLC resonant converter in its downstream architecture. Due to the characteristics of Zero Voltage Switching (ZVS) and Zero Current Switching (ZCS) inherent in LLC converters, they achieved good efficiency in their outputs. Building upon this discussion, this study proposes a high voltage gain interleaved boost series resonant converter. The converter utilizes a front-end interleaved boost converter to adjust the dead time, thereby extending the input range to a fixed voltage, while leveraging the characteristics of the interleaved boost converter to reduce current ripple. The downstream LLC resonant converter employs a transformer for voltage boosting, along with frequency modulation control to ensure stable output. Thus, the proposed converter in this study exhibits a wide input voltage range, high voltage gain, power switches, soft-switching rectifier diodes, and high conversion efficiency.

The converter presented in this paper is capable of reducing the input current ripple to 2%–5.6% of the input current under full load, regardless of whether the voltage is high or low. At 40V and 800W, it can also reduce the input current ripple to 3.75% of the input current. In contrast, the converter referenced in [24] reduces the input current ripple to 6% and 9% of the average input current, while the one in [25] achieves a reduction to 2.88% of the input current. Ideally, the converter in [26] can reduce the inductor current ripple to 2.5% of the inductor current; however, in practice, it can only reduce it to 22.8% of the inductor current. Overall, it can be observed that the converter proposed in this paper demonstrates superior performance in reducing current ripple under low voltage and full load conditions compared to references [24] ~ [26]. Table 1 presents a comparison between the converter proposed in this paper and other literature.

**Table 1. Comparison table.**

| [Ref] | Power | Efficiency | Voltage gain | Current Ripple |
|---|---|---|---|---|
| This study | 1.5kW | 92.7%-93.6% | 1.2-3.75 | 5.6%-2% |
| [1] | 65W | 84.9%-83.5% | 1 | 6%-9% |
| [2] | 1kW | 94.8% | 18.75 | 3% |
| [3] | 50W | 85.6% | 5.14 | 2.5% |

## II. THE STRUCTURE OF THE PROPOSED CIRCUIT

This paper proposes and analyzes an interleaved boost serial resonant converter with high transformation ratio. Its circuit architecture is shown in Fig. 2. In the part of the first stage interleaved boost converter, the inductors $L_1$ and $L_2$ are boost inductors, and the synchronous pulse width modulation technology (Pulse Width Modulation, PWM) is used to modulate the phases of the power switches $S_1$ and $S_2$. The working cycle of the difference 180∘controls the energy stored in the boost inductors $L_1$ and $L_2$ to achieve the function of output voltage regulation.

The second stage uses a resonant converter with soft switching. Through the full-bridge inverter composed of $S_3$~$S_6$ power switches, the DC voltage is cut into AC square waves and fed into the resonant circuit. The resonant circuit is composed of $C_r$, $L_r$, and $L_m$. The transformer transmits the energy to the load, and the AC voltage is rectified into DC voltage for the load by the $D_3$~$D_6$ rectifier circuit. In the resonant circuit, the power switch and the rectifier diode both achieve soft switching, which reduces the switching loss of the switch and thus reduces the EMI interference.

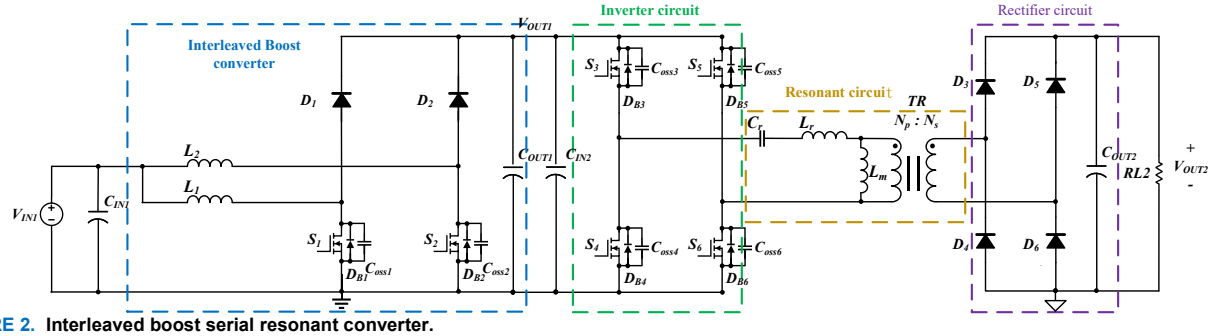


**FIGURE 2. Interleaved boost serial resonant converter.**

### A. Operating Principles

This chapter will analyze this serial converter. In order to simplify the analysis process, the whole circuit is divided into two parts: the first stage and the second stage, as shown in Fig. 3. The first stage is an interleaved boost converter, and the second stage is a LLC resonant converter.

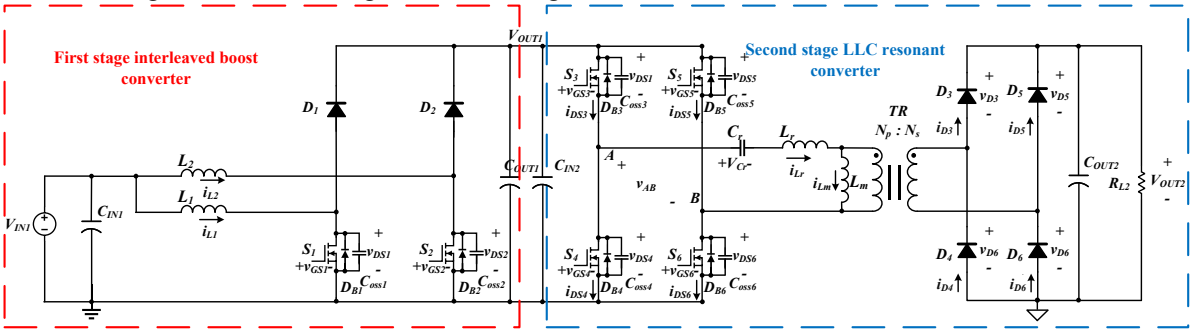


**FIGURE 3.** Circuit of interleaved boost serial resonant converter.

### B. Operation Principle of Interleaved Boost Converter

As shown in Fig. 4, the interleaved boost converter is a combination of two sets of boost circuits. The two sets of power switches $S_1$ and $S_2$ are triggered by the same duty cycle but different phase angle. Here, the duty cycle is defined as D. The two sets of driving signals $V_{GS1}$ and $V_{GS2}$ have a phase of 180° The schematic diagram of its driving signal is shown in Fig. 5. The advantage is that the input current ripple is lower and the output power can be improved.

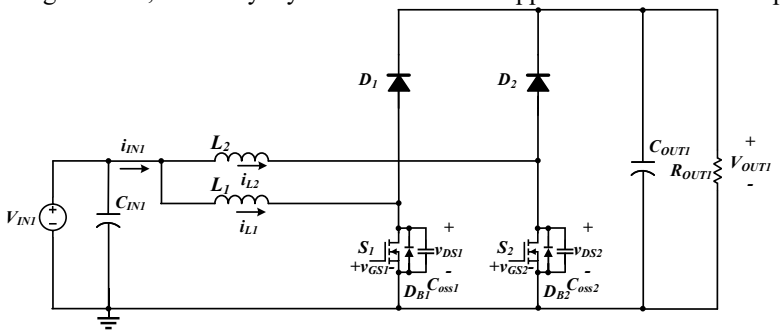


**FIGURE 4.** Circuit of interleaved boost converter.

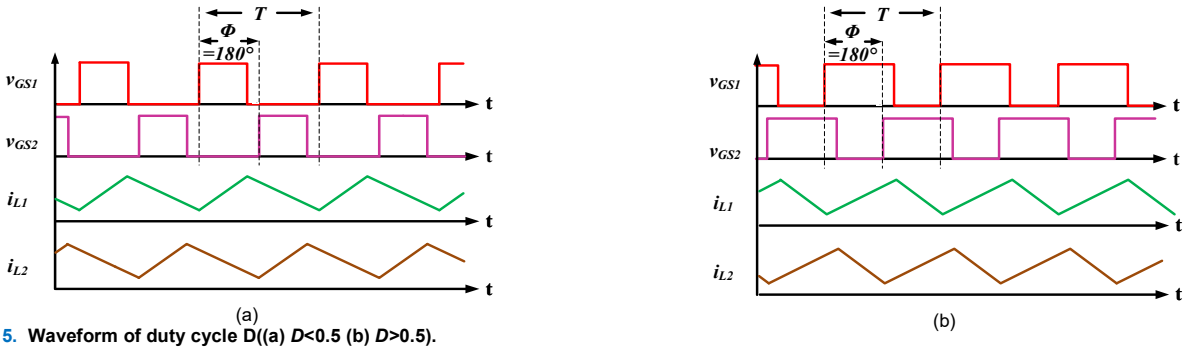


**FIGURE 5.** Waveform of duty cycle D((a) *D*<0.5 (b) *D*>0.5).

In the interleaved boost converter, when twice the input voltage is greater than the output voltage or twice the input voltage is less than the output voltage, the duty cycle D of the power switch is less than 0.5 and greater than 0.5, respectively. Since the working state of the D is less or greater than 0.5 are the same, only the D is greater than 0.5 is analyzed below. The working mode can be divided into three parts to explain:

(1) When the power switches $S_1$ and $S_2$ are both turned on, the equivalent circuit is shown in Fig. 6. The current flows from the input voltage $V_{IN1}$ through the boost inductors $L_1$ and $L_2$ for energy storage, the diodes $D_1$ and $D_2$ are reverse biased and the output is turned off. Capacitor $C_{OUT1}$ releases energy to load $R_{OUT1}$.

(2) When the power switch $S_1$ is turned on and $S_2$ is turned off, its equivalent circuit is shown in Fig. 7. At this time, the diode $D_2$ is forward biased and turned on, and the current flows from the input voltage $V_{IN1}$ through the boost inductor $L_2$ to release energy to the output capacitor $C_{OUT1}$ and the load $R_{OUT1}$, at this time the boost inductor $L_1$ is storing energy.

(3) When the power switch $S_1$ is turned off and $S_2$ is turned on, its equivalent circuit is shown in Fig. 8. At this time, the diode $D_1$ is forward biased and turned on, and the current flows from the input voltage $V_{IN1}$ through the boost inductor $L_1$ to release energy to the output capacitor $C_{OUT1}$ and the load $R_{OUT1}$, at this time, the boost inductor $L_2$ is storing energy.

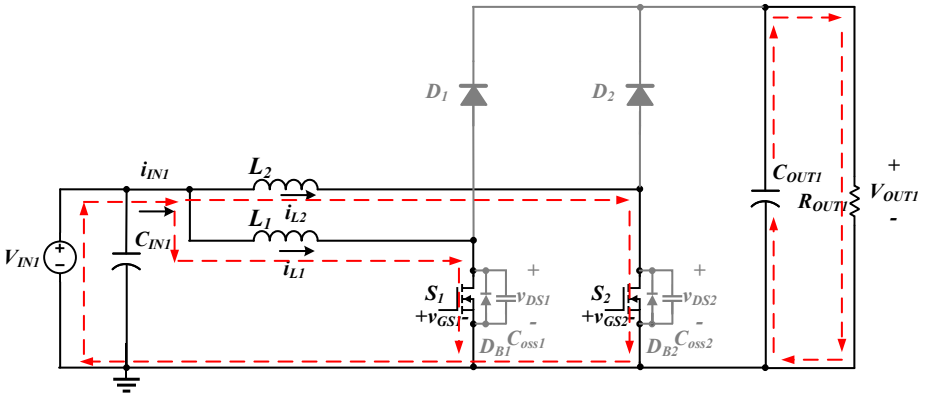


**FIGURE 6.** Power switches $S_1$ and $S_2$ are both turned on.

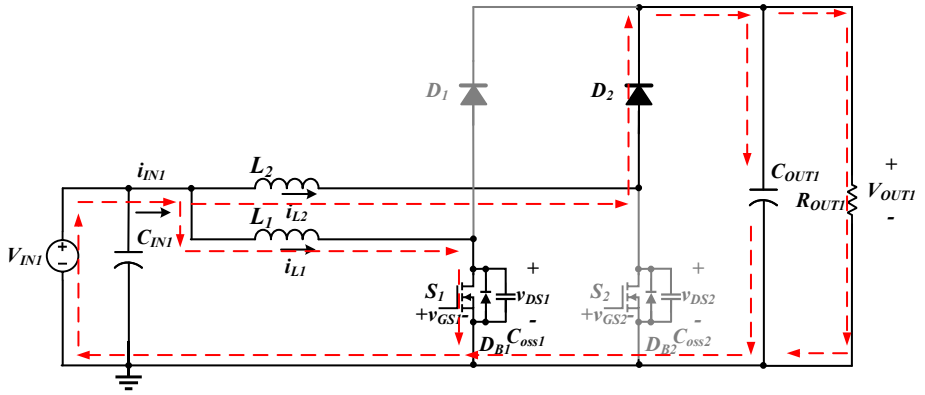


**FIGURE 7.** Power switch $S_1$ is turned on and $S_2$ is turned off.

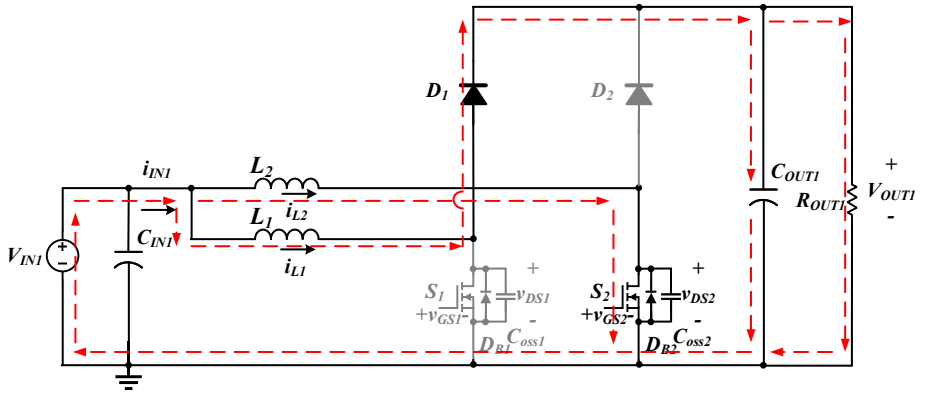


**FIGURE 8.** Power switch $S_1$ is turned off and $S_2$ is turned on.

### *C. Operating Principle of Full-bridge LLC Resonant Converter*

The LLC resonant converter circuit is shown in Fig. 9. The output voltage of the first stage interleaved boost converter is regarded as an ideal power supply $V_{IN2}$. The power switches ($S_3$, $S_6$) and ($S_4$, $S_5$) account for 50% of the complementary 180° of the duty ratio signal, the energy is transmitted to the secondary side through the resonant elements $C_r$, $L_r$, $L_m$ and the transformer, and is rectified to the output load by the secondary side diodes $D_3$~$D_6$, wherein the duty cycle still includes the dead time to prevent all switches from being turned on at the same time and causing circuit short-circuit.

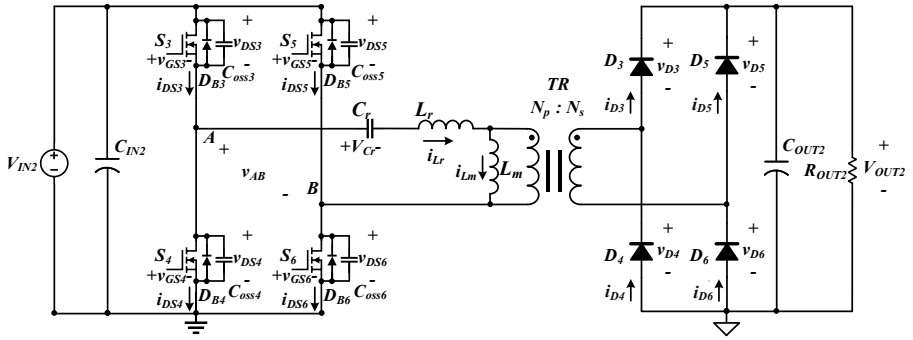


**FIGURE 9.** **Circuit of LLC resonant converter.**

Through the mathematical simulation software (Mathcad), theoretically analyze the voltage gain characteristic curve of the resonant converter, where $f_n$ is the normalized frequency, and $M_{vr}$ is the voltage gain of the resonant tank. As shown in Fig. 10 , the LLC resonant converter has a first resonance The frequency point $f_r$ is composed of $L_r$ and $C_r$, and the second resonance frequency point is $f_m$, which is composed of $L_r$, $L_m$ and $C_r$, and its expression is as follows:

$$f_r = \frac{1}{2\pi\sqrt{L_r C_r}} \tag{1}$$

$$f_m = \frac{1}{2\pi\sqrt{(L_r + L_m)C_r}} \tag{2}$$

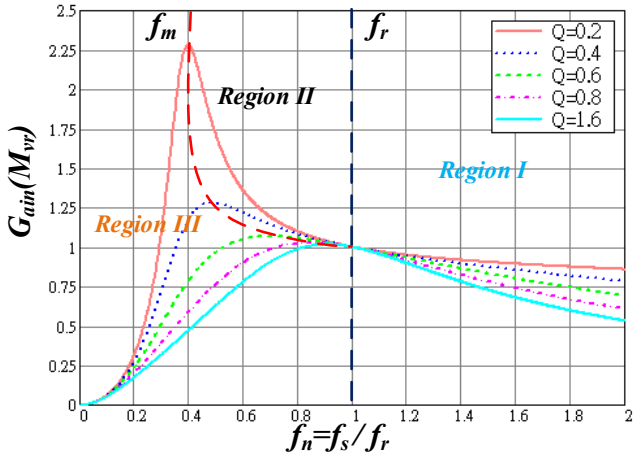


**FIGURE 10.** **Voltage Gain Characteristic Curve of Resonant Converter.**

Under the regulation of the converter frequency, the ratio of the switching frequency $f_s$ to the resonant frequency $f_r$ can be divided into the following four working states with the voltage gain characteristic curve in Fig. 10:

(1) When $f_s > f_r$, the voltage gain curve operates in Region I. At this time, the input impedance of the converter is inductive, the primary side resonant current and the excitation current are not equal in any operating range, the primary side power switch achieves ZVS, and the secondary side power switch achieves ZVS. cannot achieve the function of ZCS.

(2) When $f_s = f_r$, the voltage gain curve operates at the resonance point. At this time, $L_r$ and $C_r$ resonate in series. At this time, the input impedance of the converter is inductive. The power switch on the primary side is ZVS, and the rectifier diode on the secondary side achieves ZCS. and the voltage gain is 1 regardless of the load, which is the ideal operating point.

(3) When $f_m < f_s < f_r$, the voltage gain curve operates in Region II, and the input impedance of the converter is inductive. The primary side power switch ZVS, because the switching period is greater than the resonant period, when $L_m$ participates in the resonance, the primary The resonant current of the side is equal to the excitation current. At this time, the transformer enters the decoupling interval. During the decoupling interval, the primary side cannot transfer energy to the negative secondary side. The rectifier diode current on the secondary side naturally drops to zero and reaches ZCS. Features that can achieve soft switching.

(4) When $f_s < f_r$, the voltage gain curve operates in Region III. At this time, the input impedance of the converter is capacitive, and the primary side power switch cannot ZVS, and the voltage gain changes greatly with the switching frequency in this region, which is not easy to control, the converter operation should be avoided in this mode.

In this paper, the second stage resonant circuit belongs to a unidirectional fixed output and input voltage. In order to make the primary side and the secondary side have soft switching, the converter is designed to operate in Region II, so the work flow of frequency conversion control for the converter operating in Region II operating principle. Fig. 11 is the ideal waveform of the converter operating in Region II, and the voltage and current directions of the circuit are defined in Fig. 9. According to the switching state of the power switch, one cycle of the power switch signal can be divided into 10 working modes. Since the working state of the positive half cycle and negative half cycle are the same, only the positive half cycle is analyzed below.

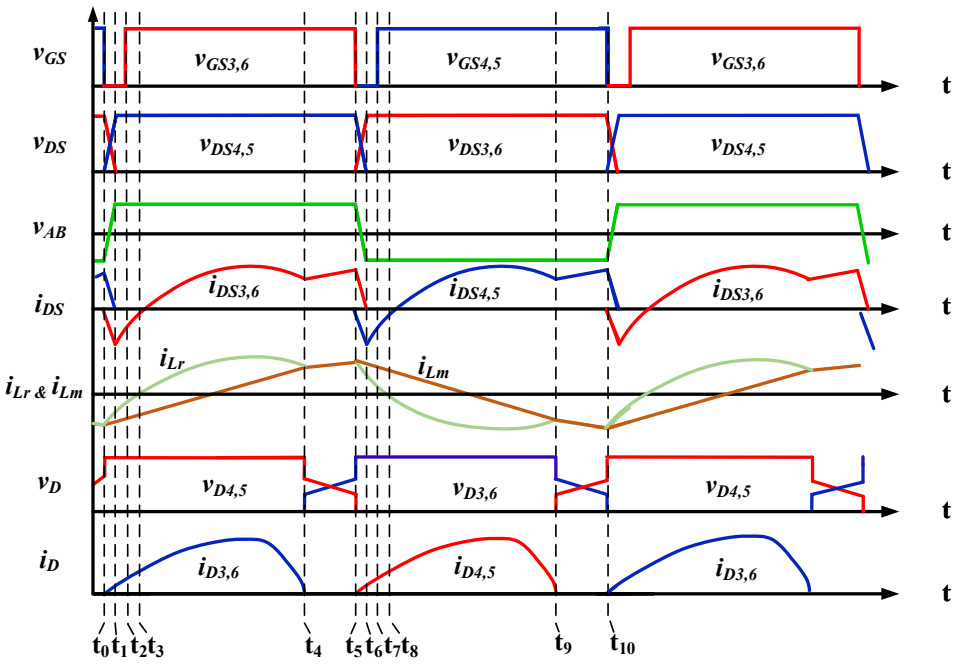


FIGURE 11. Ideal waveform of the converter operating in Region II.

### 1). Operating Stage I ($t_0 < t \le t_1$)

As shown in Fig. 12, when t=$t_0$, the power switches $S_4$ and $S_5$ are turned off. At this time, the power switches $S_3$~$S_6$ are all turned off, the primary side full-bridge power switch enters the dead time state, and the resonant current $i_{Lr}$ begins to store energy for the parasitic capacitances $C_{oss4}$ and $C_{oss5}$ of the power switches $S_4$ and $S_5$, and also releases the energy for the parasitic capacitances $C_{oss3}$ and $C_{oss6}$ of the power switches $S_3$ and $S_6$. The secondary side rectifier diode is $D_3$ and $D_6$ is turned on, and $D_4$ and $D_5$ are turned off. Through the design of dead time, the energy storage and release time of the parasitic capacitors is less than the dead time to ensure the ZVS of the switch. When the parasitic capacitances $C_{oss4}$ and $C_{oss5}$ are charged to $V_{IN2}$, and the parasitic capacitances $C_{oss3}$ and $C_{oss6}$ are discharged to 0V, this mode ends.

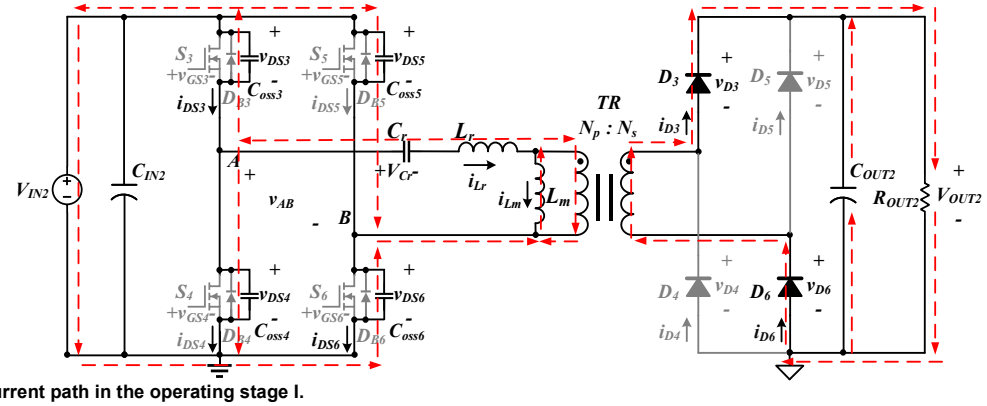


FIGURE 12. The current path in the operating stage I.

### 2). Operating Stage II ($t_1 < t \le t_2$)

As shown in Fig. 13, when t=$t_1$, the power switches $S_3$~$S_6$ are all turned off. After the parasitic capacitors are charged and discharged, the resonant current $i_{Lr}$ discharges the parasitic capacitances $C_{oss3}$ and $C_{oss6}$ to 0V, and then freewheels through the body diode on the power switch to make the power switches $S_3$ and $S_6$ reach the condition of ZVS. At the same time, $i_{Lr}$ transmits energy to the secondary side through the transformer, the secondary side rectifier diodes $D_3$ and $D_6$ are turned on, and $D_4$ and $D_5$ are turned off. When t=$t_2$, the power switches $S_3$ and $S_6$ are turned on and enter the next working mode.

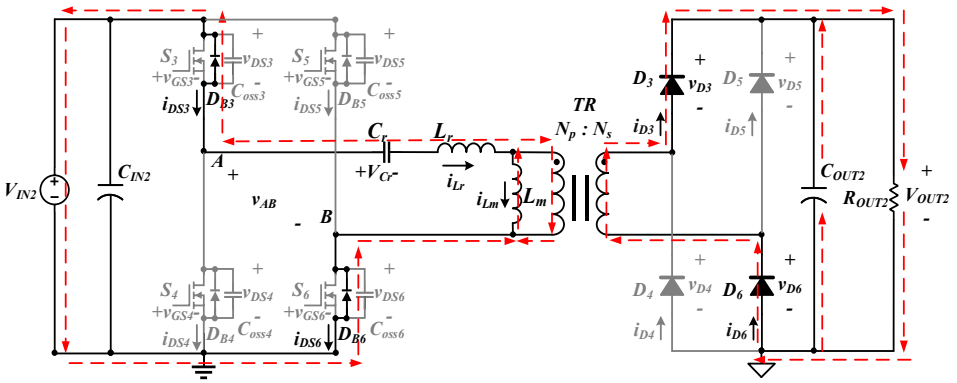


**FIGURE 13.** The current path in the operating stage II.

### 3). Operating Stage III ($t_2 < t \leq t_3$)

As shown in Fig. 14, when $t = t_2$, the power switches $S_3$ and $S_6$ are turned on, the power switches realize ZVS, and the power switches $S_4$ and $S_5$ are turned off. At this time, $i_{Lr}$ and $i_{Lm}$ continue to rise, and the energy is transferred to the secondary side through the transformer, and the secondary side rectifier diodes $D_3$ and $D_6$ are turned on to provide the energy to the load. The magnetizing inductor $L_m$ does not participate in the resonance due to the clamping effect of the output voltage $V_{OUT2}$, and the magnetizing inductor current $i_{Lm}$ continues to rise. When the resonant current $i_{Lr} = 0$, this mode ends.

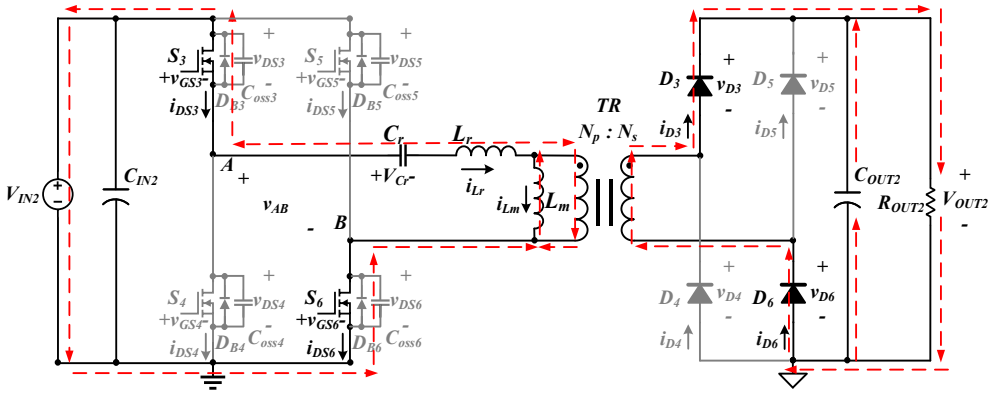


**FIGURE 14.** The current path in the operating stage III.

### 4). Operating Stage IV ($t_3 < t \leq t_4$)

As shown in Fig. 15, when $t = t_3$, the power switches $S_3$ and $S_6$ are still turned on, and the resonant current $i_{Lr}$ changes from negative to 0. At this time, $C_r$ and $L_r$ resonate, so that the resonant current $i_{Lr}$ increases the current difference between the magnetizing current $i_{Lm}$ through the secondary side of the transformer to transmit energy, and the secondary side rectifier diodes $D_3$ and $D_6$ are turned on to provide load energy, and the magnetizing inductor $L_m$ does not participate in the resonance due to the clamping effect of the output voltage $V_{OUT2}$, the magnetizing inductor current $i_{Lm}$ continues to rise from negative to positive until when the resonant current $i_{Lr}$ is equal to the magnetizing current $i_{Lm}$, this mode ends. At the same time, the rectifier diode current $i_{D3}$ and $i_{D6}$ are also reduced to 0A, which achieves the condition of ZCS.

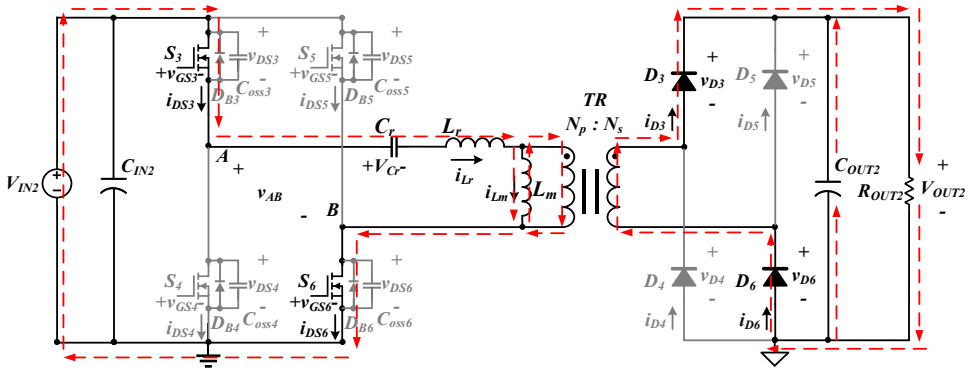


**FIGURE 15.** The current path in the operating stage III.

**5). Operating Stage V ($t_4 < t \leq t_5$)**

As shown in Fig. 16, when $t = t_4$, the power switches $S_3$ and $S_6$ are still turned on, the power switches $S_4$ and $S_5$ are turned off, and the resonant current $i_{Lr}$ is equal to the magnetizing current $i_{Lm}$. At this time, the transformer enters the decoupling interval without providing energy, and the rectifier diode current $i_{D3}$ and $i_{D6}$ are naturally turn off to achieve ZCS. Since the transformer doesn't transmit energy to the load, the magnetizing inductor $L_m$ is not affected by the clamping of the output voltage $V_{OUT2}$, so $L_r$ and $C_r$ resonate with $L_m$ in this interval. Until $t = t_5$, the power switches $S_3$ and $S_6$ are turned off, this mode ends.

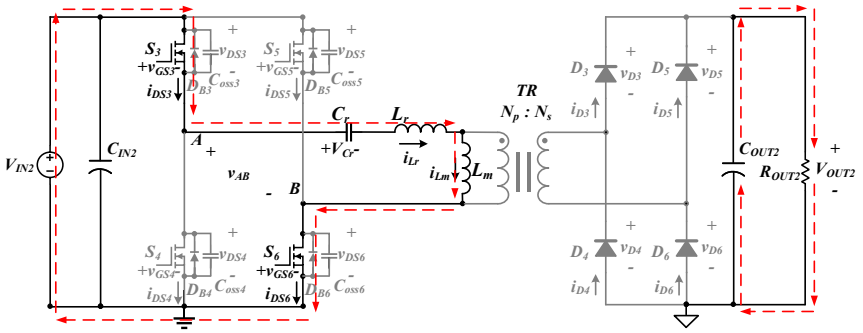


**FIGURE 16.** **The current path in the operating stage V.**

### *D. Input Current Ripple*

In this paper, the first stage interleaved boost converter analyzes its input current ripple from the input side, as shown in Fig. 17. The figure shows the input current in the two cases when the duty cycle $D \leq 0.5$ and the duty cycle $D > 0.5$, respectively. The difference between the switch driving signals is 180° out of phase, so that the two-phase inductor currents $i_{L1}$ and $i_{L2}$ also have a 180° phase difference. Therefore, after the two-phase inductor currents are added, the current ripples cancel each other out, and the total input current $i_{IN1}$ has a reduced ripple, and the current frequency is twice of the switch.

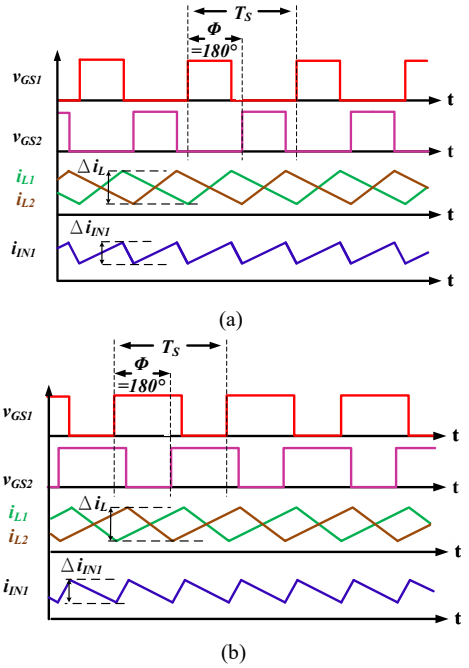


**FIGURE 17.** **Waveform of input current ((a) *D* < 0.5(b) > 0.5).**

Ignoring any external factors, the inductor value $L = L_1 = L_2$, the two-phase inductor current ripple is equal, so the current ripple of each phase is as follows:

$$\Delta i_L = \Delta i_{L1} = \Delta i_{L2} = \frac{V_{IN1} D}{f_s L} \tag{3}$$

The total input current is equal to the sum of the two-phase inductor currents, $i_{IN1} = i_{L1} + i_{L2}$, when $D \leq 0.5$, the total input current ripple $\Delta i_{IN1}$ is:

$$\Delta i_{IN1} = \frac{V_{IN1}(1-2D)DT_s}{(1-D)L} \tag{4}$$

For $D > 0.5$, the total input current ripple $\Delta i_{IN1}$ is:

$$\Delta i_{IN1} = \frac{V_{IN1}(2D-1)T_s}{L} \tag{5}$$

According to equations (3), (4) and (5), equation (6) can be obtained, where λ is the ripple coefficient used to represent the total input current ripple suppression capability.

$$\lambda = \frac{\Delta i_{IN1}}{\Delta i_L} = \begin{cases} \dfrac{1-2D}{1-D}, & D \leq 0.5 \\ \dfrac{2D-1}{D}, & D > 0.5 \end{cases} \tag{6}$$

Through equations (6), the relationship between the λ and D can be known as shown Fig. 18.

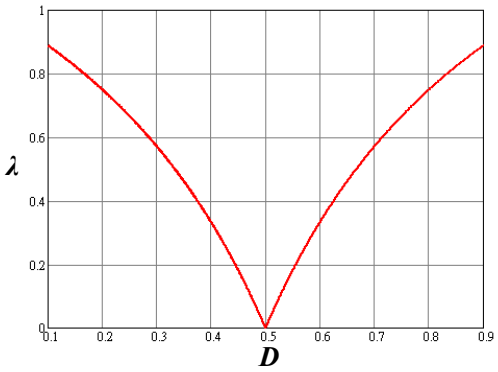


FIGURE 18. Curve of $\lambda$ and D.

### E. Circuit Gain Analyze

The inductor current of the first stage interleaved boost converter is in continuous conduction mode (CCM), while the two-phase interleaved operating mode is the same, only a phase difference of 180 degrees. When analyzing the voltage gain, only one of the phases is selected for analysis. Its equivalent is shown in Fig. 19.

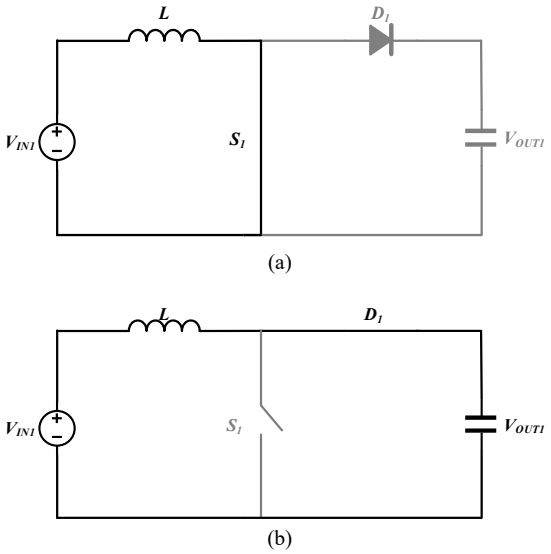


FIGURE 19. Single-phase equivalent circuit (a) $S_1$ on (b) $S_1$ off.

From Fig. 19, when the converter is in steady state, within one switching cycle, the following formula is listed according to the principle of volt-second balance:

$$V_{IN1}DT_s = (V_{IN1} - V_{OUT1}) \cdot (1 - D)T_s \tag{7}$$

First-stage interleaved boost converter voltage gain:

$$G_1 = \frac{V_{OUT1}}{V_{IN1}} = \frac{1}{1 - D} \tag{8}$$

The voltage gain of the second stage LLC resonant converter is based on the FHA analysis method to establish an AC equivalent circuit model, which converts the equivalent resistance of the secondary side output end to the primary side, and the transformer turns ratio is N, as shown in Fig. 20.

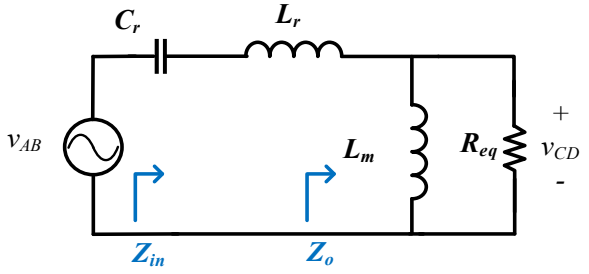


FIGURE 20. LLC equivalent circuit model.

The voltage gain can be expressed by the input impedance and output impedance as:

$$M_{vr}(\mathrm{s}) = \frac{v_{CD}(s)}{v_{AB}(s)} = \frac{Z_o(s)}{Z_{in}(s) + Z_{o(s)}} \tag{9}$$

The impedance expressions are as follows:

$$Z_{in}(s) = sL_r + \frac{1}{sC_r}$$

$$Z_o(s) = sL_m \| R_{eq} \tag{10}$$

$$R_{eq} = \frac{8}{\pi^2} N^2 R_{OUT2}$$

In this paper, $f_s$ is defined as the switching frequency of the power switch, $f_r$ is the frequency of the first resonance point, the normalized frequency $f_n$ is the ratio of $f_s$ to $f_r$, Q is the quality factor, and k is the ratio of $L_m$ to $L_r$. The expressions are as follows.

$$f_r = \frac{1}{2\pi\sqrt{L_r C_r}} \tag{11}$$

$$f_n = \frac{f_s}{f_r} \tag{12}$$

$$Q = \frac{\sqrt{\frac{L_r}{C_r}}}{R_{eq}} \tag{13}$$

$$k = \frac{L_m}{L_r} \tag{14}$$

Bringing the above definition into equation (9), the simplified voltage gain can be obtained as:

$$M_{vr}(f_n) = \frac{1}{\sqrt{(1+\frac{1}{k}-\frac{1}{kf_n^2})^2 + Q^2(f_n-\frac{1}{f_n})^2}} \tag{15}$$

The voltage gain $G_2$ of the second stage resonant converter is:

$$G_2 = \frac{M_{vr}(f_n)}{N} \tag{16}$$

## III. Design Procedure and Consideration

The design is based on the specifications required in this paper, and the parameters are calculated and verified from the electrical specifications of the converter Table 2. Due to the use of a two-stage structure, the following parameters are designed for the first and second stages respectively. The design process is shown in Fig. 21.

**Table 2. Specifications of this Converter.**

| Parameters | Specifications |
|---|---|
| $V_{IN1}$ (Primary) | 40~125V |
| $V_{OUT1}$ (Primary) | 150V |
| $V_{IN2}$ (Secondary) | 150V |
| $V_{OUT2}$ (Secondary) | 400V |
| P (Rated power) | 1.5 kW |
| $f_r$ (Resonant freq.) | 100 kHz |
| $f_s$ (Switching freq.) | 81 kHz ~100kHz |

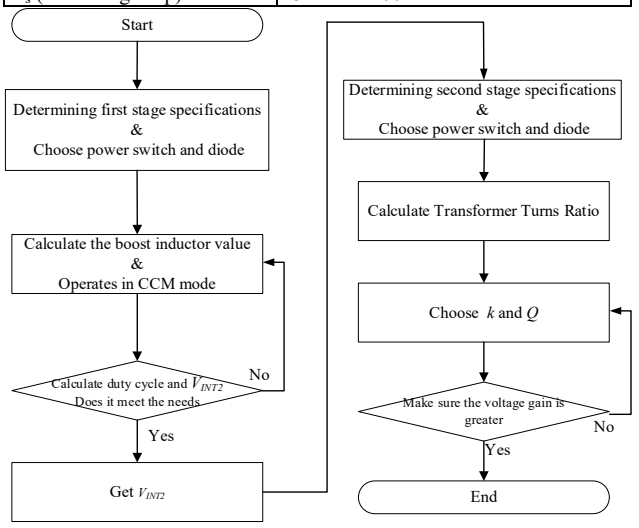


**FIGURE 21. Design Procedures for this Converter.**

### 1). Step 1. Parameters for key Components

In this study, the power switches are the key components of the proposed converter. Table 3 shows the rated values of the switches to meet the specifications of the converter. The related parameters are list as follow.

**Table 3. Specification and rated value of power switch.**

| Parameters | Value |
|---|---|
| $V_{DS\ MAX}$ | 650V |
| $I_{DS\ MAX}$ | 85A |
| $C_{OSS}$ | 320pF |
| $V_{RRM}$ | 600V |
| $I_{FAV}$ | 60A |
| $V_F$ | 1.75V |

### 2). Step 2. Calculate the Boost Inductor Value

From Fig. 22, the minimum value of the inductor current must be greater than or equal to 0 when operating in CCM mode. Here, the $V_{IN1}$ and $V_{OUT1}$ of the fuel cell terminal are selected, and the output power of a single phase is 750W as the design basis, and the inductance value is calculated, which can be calculated from the following equation.

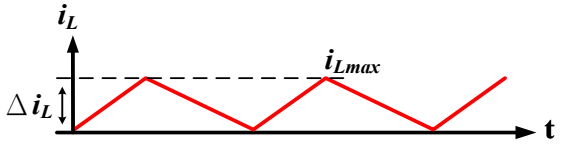


**FIGURE 22. Inductor current in Boundary mode.**

$$D_{min} = \frac{V_{OUT1} - V_{IN1\_max}}{V_{OUT1}} = \frac{150-125}{150} \cong 0.166$$
$$D_{max} = \frac{V_{OUT1} - V_{IN1\_min}}{V_{OUT1}} = \frac{150-40}{150} \cong 0.733 \tag{17}$$

Substitute equation (17) D into the following equation to obtain the minimum inductance value operating in CCM mode:

$$L_{125\_min} \geq \frac{30(1-0.166)^2}{2} \times 0.166 \times 10^{-5} \cong 17.3\mu H$$
$$L_{40\_min} \geq \frac{30(1-0.733)^2}{2} \times 0.733 \times 10^{-5} \cong 7.83\mu H \tag{18}$$

In order to ensure that the load can be operated in CCM mode from light load to full load, the value of the boost inductor is usually selected to be 2~15 times of the full load calculation:

$$L_1 = L_2 = 13 \times L_{125\_min} \cong 225\mu H \tag{19}$$

The final actual wound boost inductance value is about 250μH.

### 3). Step 3. Ratio of Transformer Turns Design

Select the $V_{IN2}$ and $V_{OUT2}$ value for transformer design as shown in the following equation:

$$N = \frac{N_P}{N_S} = \frac{V_{IN2}}{V_{OUT2}} = \frac{150}{400} = 0.375 \cong 0.4 \tag{20}$$

### 4). Step 4. Voltage Gain of the Resonant Tank

Step3 calculation can obtain the transformer turns ratio of 0.4, and then use the following formula to obtain the voltage gain that needs to be supplemented by the resonant tank:

$$M_{vr} = \frac{N \cdot V_{OUT2}}{V_{IN2}} = \frac{0.4 \cdot 400}{150} = 1.066 \cong 1.07 \qquad (21)$$

### 5). Step 5. Choose *Q*, *k* Values

According to equation (15), in order to satisfy the premise of the voltage gain of the converter, since the Q value will be affected by the output load, when the parameter k is fixed, the curve conforming to each load must be selected. Therefore, the maximum output load power voltage is 400V/ 3.75A is the design standard. Choose k=6 and Q=0.45 as the design of the voltage gain curve of the converter as shown in Fig. 23.

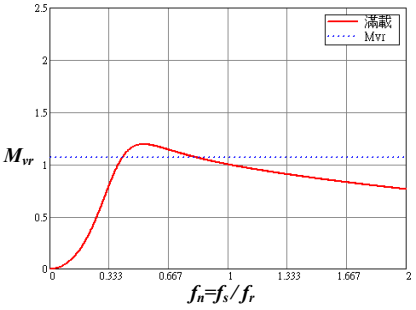


**FIGURE 23.** Voltage gain curve under full load.

### 6). Step 6. Calculate the Resonance Parameter Value

After the Q and k values are selected, the parameter values of each resonance element can be obtained as shown in the following equation.

$$R_{eq} = \frac{8}{\pi^2} \cdot N^2 \cdot \frac{V_{OUT2}}{I_{OUT2}} = \frac{8}{\pi^2} \cdot 0.4^2 \cdot \frac{400}{3.75} \cong 13.83\Omega \qquad (22)$$

$$C_r = \frac{1}{2\pi \cdot f_r \cdot R_{eq} \cdot Q} = \frac{1}{2\pi \cdot 100\text{k} \cdot 13.83 \cdot 0.45} \cong 255.7nF \qquad (23)$$

$$L_r = \frac{1}{(2\pi \cdot f_r)^2 \cdot C_r} = \frac{1}{(2\pi \cdot 100\text{k})^2 \cdot 255.7n} \cong 9.9\mu H \qquad (24)$$

$$L_m = L_r \cdot k = 9.9\mu \cdot 6 \cong 59.4\mu H \qquad (25)$$

### *A. DSP Controller*

### 1). System Architecture

In this paper, the digital signal processor TMS320F28335 developed by Texas Instruments is used as the control core of the converter system. It generates and monitors the output voltage through the switch driving signal, as shown in Fig. 24. The A/D conversion module is used to convert the external analog voltage into VADC for digital signal conversion for compensation, and the ePWM module is used to generate the corresponding pulse wave of the switch driving signal to stabilize the output voltage of the converter

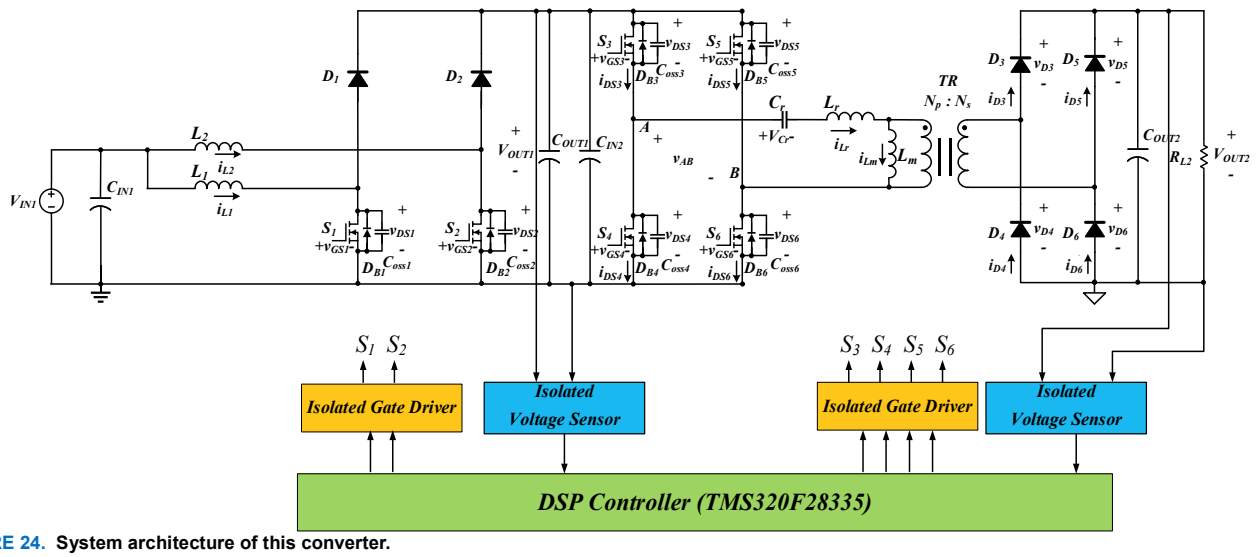


**FIGURE 24.** System architecture of this converter.

### 2). Design of DSP

Fig. 24 is a system architecture of this converter. The first stage interleaved boost converter and the second stage full-bridge LLC resonant circuit are respectively used for feedback control. The system control block diagram is shown in Fig. 25.

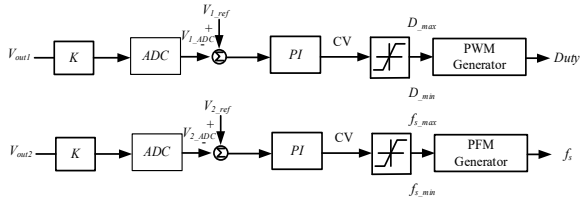


**FIGURE 25. System control block.**

## IV. Simulation and Analysis

This section verifies the overall feasibility of the circuit through simulation and analysis conducted using PSIM software developed by Powersim.

### *A. First Stage Low-voltage Input Mode Simulation Waveform*

As shown in Fig. 26, the simulated converter operates in low-voltage input mode, with an input voltage of $V_{IN1}$ = 40 V and an output voltage of $V_{OUT1}$ = 150 V. Fig. 26 illustrates the simulated waveforms of $i_{IN1}$, $i_{L1}$, $i_{L2}$, $V_{GS1}$ for the interleaved boost converter under light load (200 W), medium load (800 W), and full load (1.5 kW).

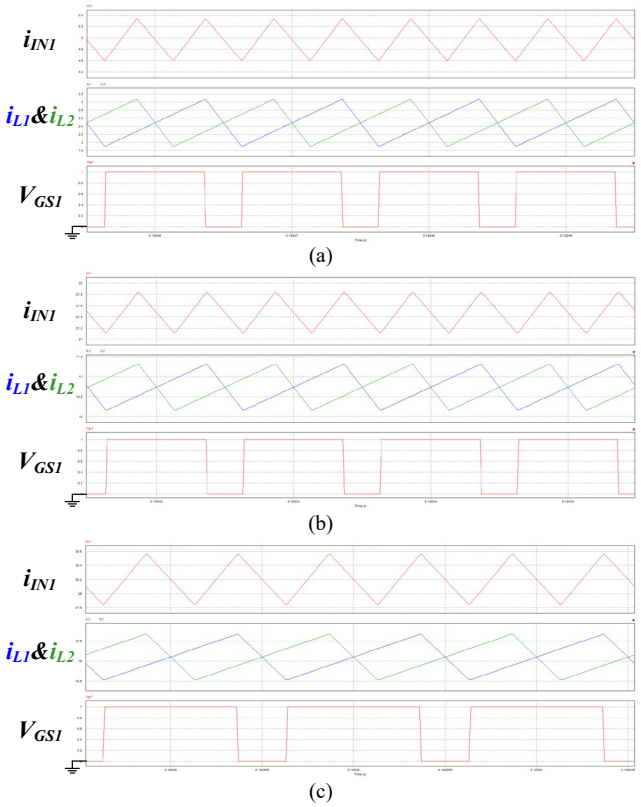


**FIGURE 26. Simulated waveform of low-voltage input mode((a) 200W (b) 800W (c) 1.5kW).**

### *B. First Stage High-voltage Input Mode Simulation Waveform*

As shown in Fig. 27, the simulated converter operates in high-voltage input mode, with an input voltage of $V_{IN1}$ = 125 V and an output voltage of $V_{OUT1}$ = 150 V. Fig. 27 illustrates the simulated waveforms of $i_{IN1}$, $i_{L1}$, $i_{L2}$, $V_{GS1}$, and for the interleaved boost converter under light load (200 W), medium load (800 W), and full load (1.5 kW).

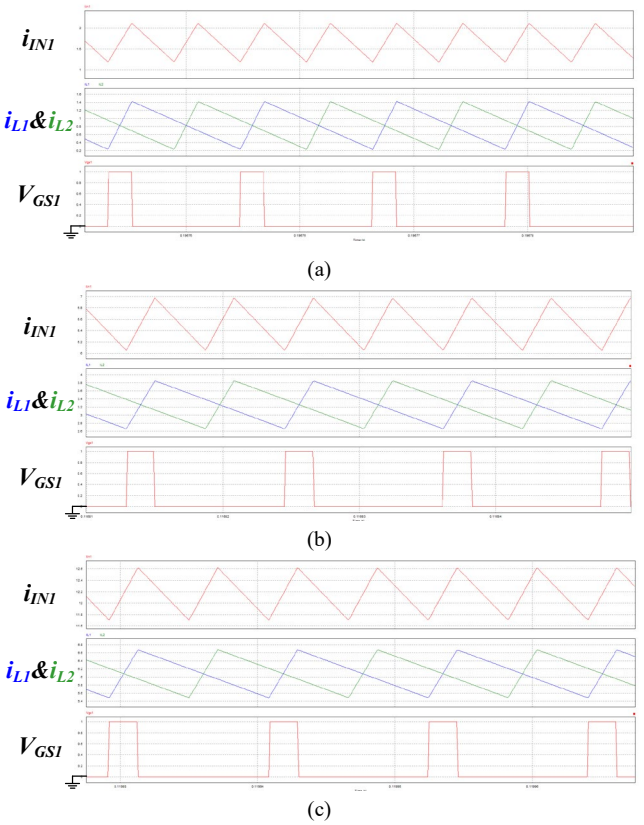


**FIGURE 27. Simulated waveform of high-voltage input mode((a) 200W (b) 800W (c) 1.5kW).**

### *C. Second Stage Power Switch S3 Simulation Waveform*

As shown in Fig. 28, the simulation of the converter operates under light load of 200W, medium load of 800W, and full load of 1.5kW. The input voltage for the output full-bridge LLC resonant converter is $V_{IN2}$ = 150V, and the output voltage is $V_{OUT2}$ = 400V. The power switch S3 switching signal $V_{GS3}$, switching voltage $V_{DS3}$, and switching current $i_{DS3}$ are depicted in Fig. 28. It can be observed that when the power switch $V_{GS3}$ is conducting, the switching current $i_{DS3}$ exhibits negative current, which allows the energy stored in the parasitic capacitance of the switch to be released. Additionally, continuous current is facilitated by the body diode. When $V_{GS3}$ is conductive, the zero-voltage switching (ZVS) function is achieved.

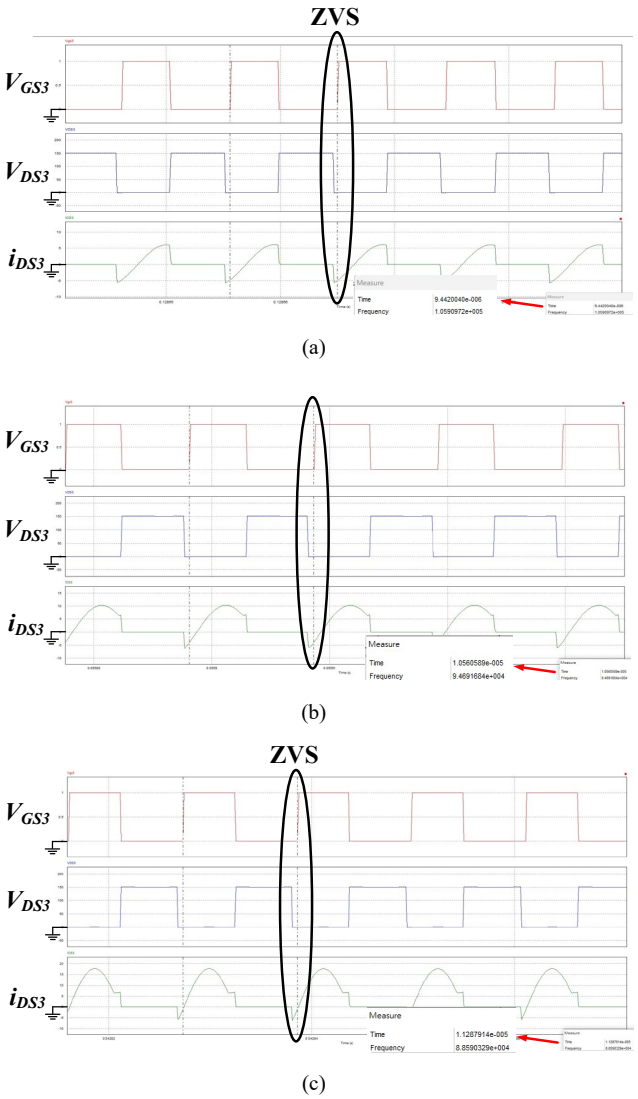


**FIGURE 28.** Simulated Waveform of $V_{GS3}$, $V_{DS3}$ and $i_{DS3}$ ((a) 200W (b) 800W (c) 1.5kW).

### *D. Second Stage Diode D3 Simulation Waveform*

As shown in Fig. 29, the simulation of the converter operates under light load of 200W, medium load of 800W, and full load of 1.5kW. As shown in Fig. 29, the rectifier diode D3 exhibits the voltage across its terminals $V_{D3}$ and the current $i_{D3}$. At this point, the converter operates in Region II where the transformer enters the decoupling phase, and no energy is transferred to the rectifier side. Consequently, before the diode turns off, the rectifier current $i_{D3}$ naturally decreases to 0 A, achieving zero-current switching (ZCS) when $V_{D3}$ is blocked.

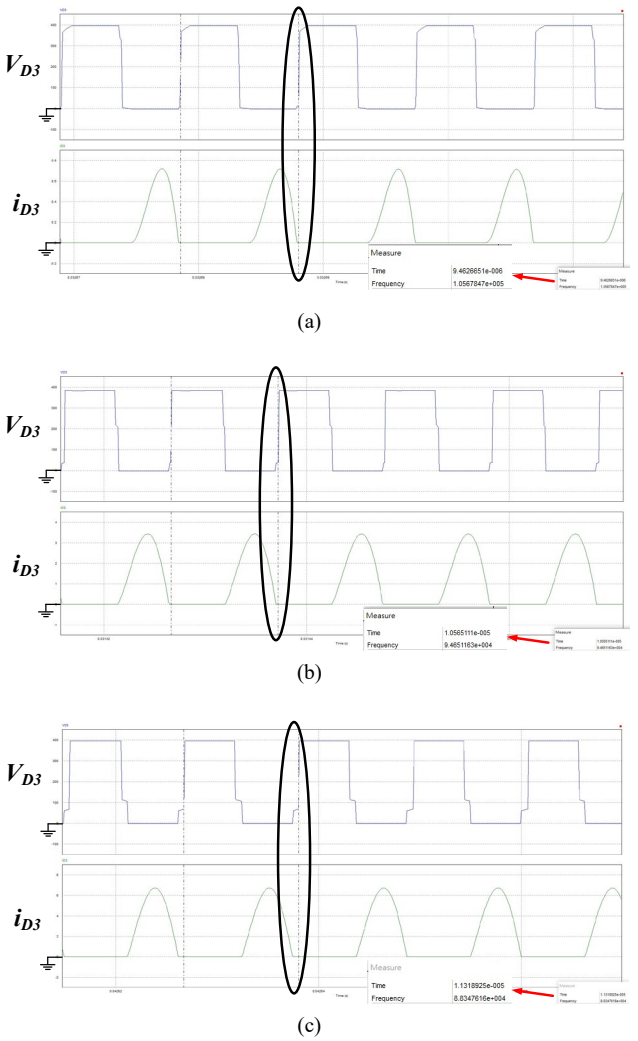


**FIGURE 29.** Simulated Waveform of $V_{D3}$ and $i_{D3}$ ((a) 200W (b) 800W (c) 1.5kW).

## V. Experimental Results

As shown in Table 4, the circuit parameters and component is chosen in this article. The converter is designed according to the circuit parameter design and component chosen in the previous chapters.

**Table 4.** Specifications for this Converter.

| Parameters | Value / Models |
|---|---|
| $N_p : N_s$ | 0.4 : 1 |
| $L_1$ | 250μ$H$ |
| $L_2$ | 250μ$H$ |
| $L_m$ | 59.8μH |
| $L_r$ | 9.9μ$H$ |
| $C_r$ | 251.5n$F$ |
| $C_{OUT1}$ | 680μF |
| $D_1$~$D_6$ | DSEI60-06A |
| $S_1$~$S_6$ | UJ3C065030K3S |
| *Dsp* | TMS320F28335 |

### *A. First Stage Low-voltage Input Mode Measurement Waveform*

Fig. 30 shows the measured waveform of the first stage converter operating in low-voltage input mode with light load of 200W, medium load of 800W and full load of 1.5kW, the input voltage is $V_{IN1}$=40V, and the output voltage is $V_{OUT1}$=150V.

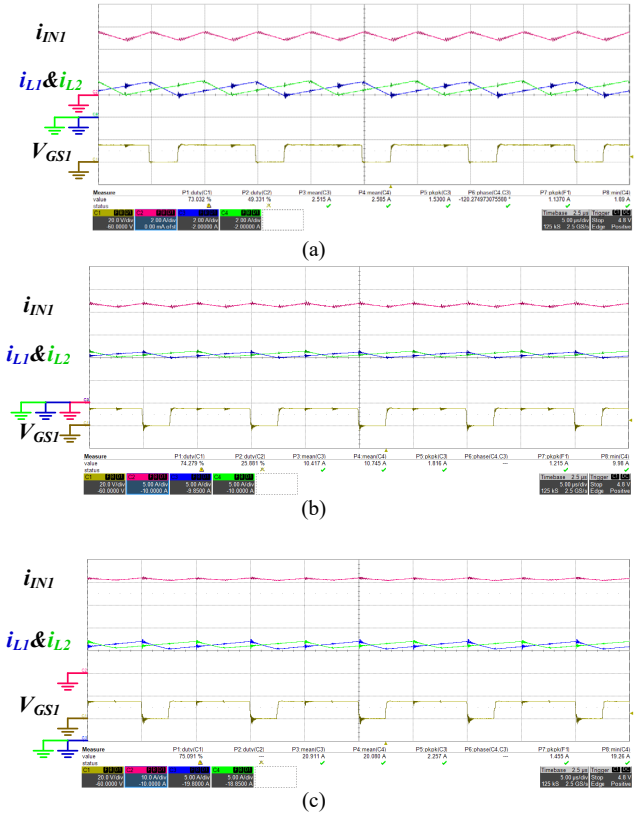


**FIGURE 30. Waveform of low-voltage input mode((a) 200W (b) 800W (c) 1.5kW).**

### *B. First Stage High-voltage Input Mode Measurement Waveform*

Fig. 31 shows the measured waveform of the first stage converter operating in high-voltage input mode with light load of 200W, medium load of 800W and full load of 1.5kW, the input voltage is $V_{IN1}$=125V, and the output voltage is $V_{OUT1}$=150V.

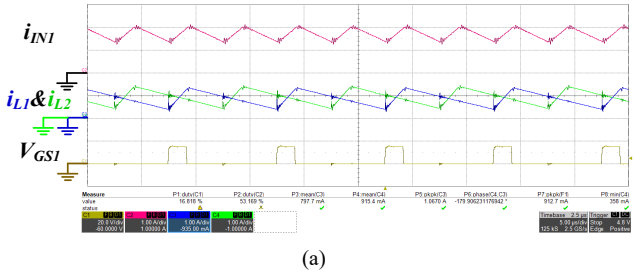


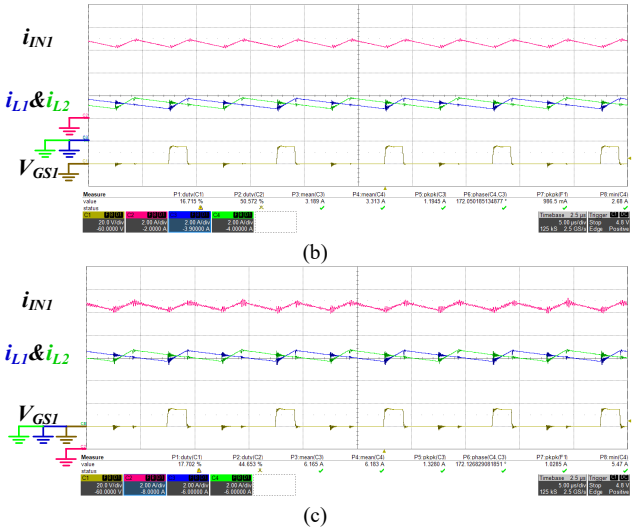


**FIGURE 31. Waveform of high-voltage input mode((a) 200W (b) 800W (c) 1.5kW).**

### *C. Second Stage Power Switch S3 Measurement Waveform*

As shown in Fig. 32, when the converter is under light load of 200W, medium load of 800W and full load of 1.5kW, the switching signal $V_{GS3}$, switching voltage $V_{DS3}$ and switching current $i_{DS3}$ of $S_3$, it can be found that when the switch $V_{GS3}$ is turned on, the current $i_{DS3}$ is negative. The current discharges the parasitic capacitance energy on the switch, and achieves freewheeling through the body diode, and realizes the zero voltage switching function when $V_{GS3}$ is turned on.

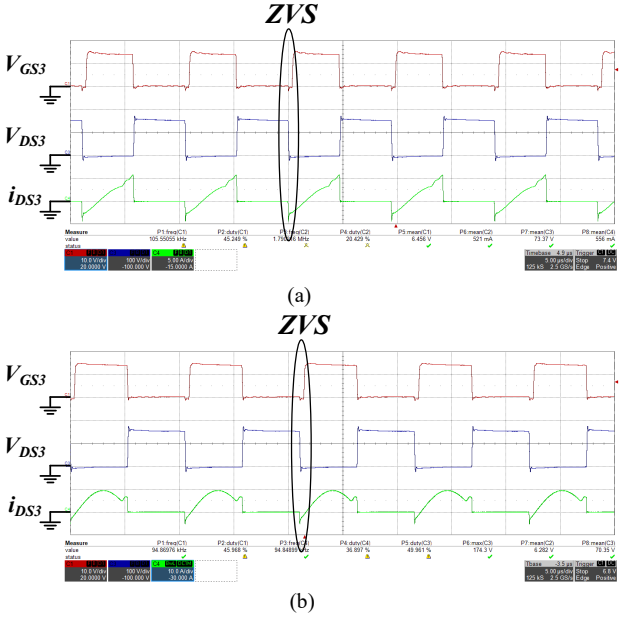

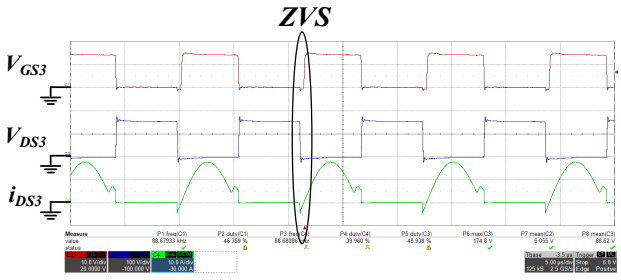


(c)

**FIGURE 32. Waveform of $V_{GS3}$, $V_{DS3}$ and $i_{DS3}$ ((a) 200W (b) 800W (c) 1.5kW).**

### *D. Second Stage Voltage and Current of Resonant Tank Measurement Waveform*

As shown in Fig. 33, when the converter has a light load of 200W, a medium load of 800W and a full load of 1.5kW, it can be seen from the figure that the second stage full-bridge switch generates a square wave input voltage $V_{AB}$ of $+V_{IN2}$ and $-V_{IN2}$, while the resonant current $i_{Lr}$ lags the resonance When the voltage $V_{AB}$ in front of the slot is inductive, the circuit can help the power switch to realize the zero voltage switching function. When the excitation current $i_{Lm}$ is the same as the resonant current $i_{Lr}$, the transformer enters the decoupling range, so that the rectifier and measuring diode realize the zero current switching function.

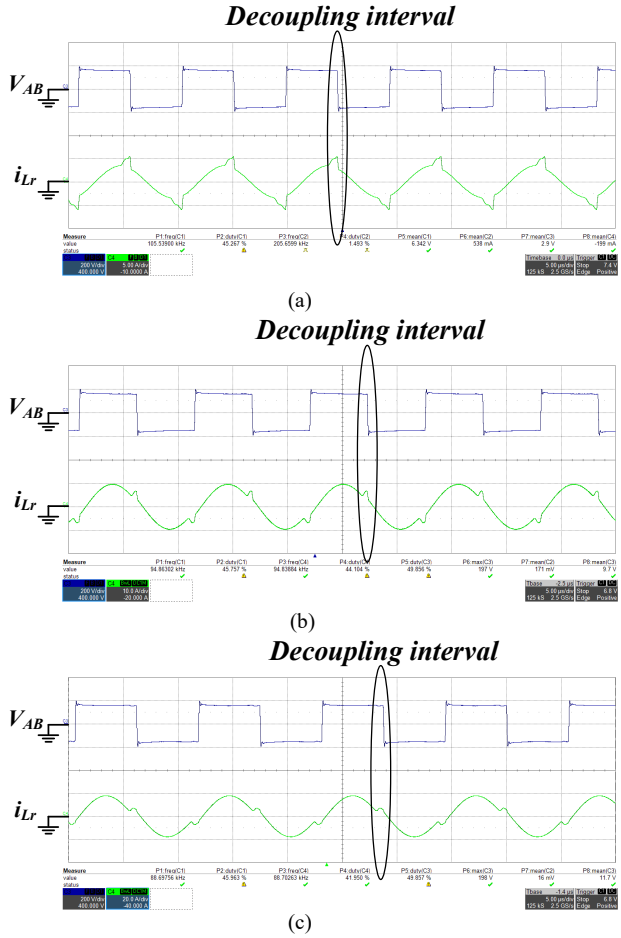


**FIGURE 33. Waveform of $V_{AB}$ and $i_{Lr}$ ((a) 200W (b) 800W (c) 1.5kW).**

### *E. Second Stage Diode D3 Measurement Waveform*

Fig. 34 shows the waveforms of the diode voltage $V_{D3}$ and current $i_{D3}$ on the rectifier side when the converter is light load 200W, medium load 800W and full load 1.5kW. The current on the rectifier side is naturally reduced to 0A, so that the rectifier diode can realize the zero current switching function.

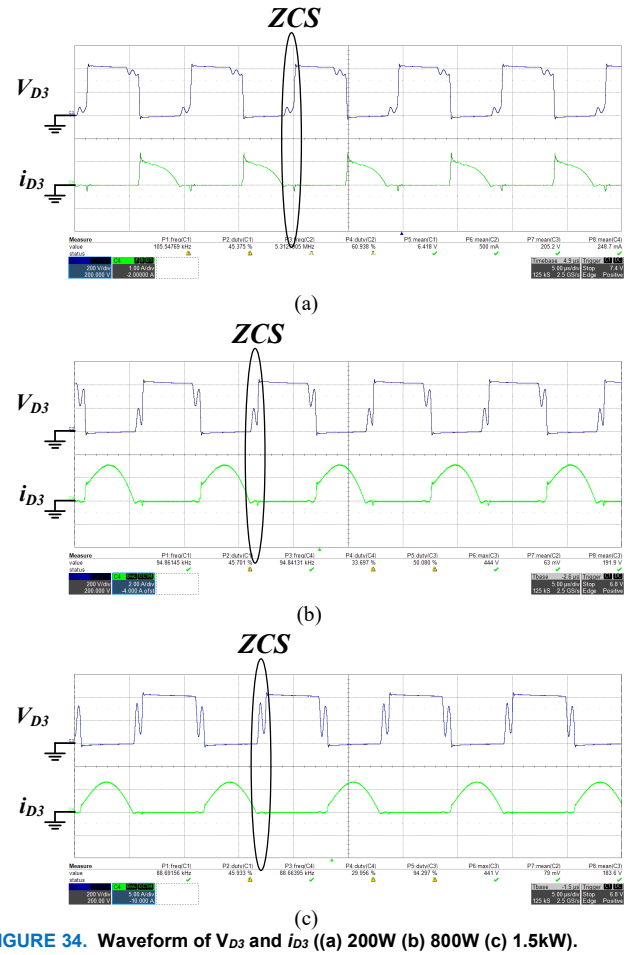


**FIGURE 34. Waveform of $V_{D3}$ and $i_{D3}$ ((a) 200W (b) 800W (c) 1.5kW).**

### *F. Load Variation Test*

Fig. 35 is a schematic diagram of the converter's experimental serial structure. Fig. 36 and Fig. 37 are the waveform of load variation in the low and high voltage input modes, respectively. After compensation by the proportional integral controller, the corresponding drive signal is generated to send to the main circuit to regulate voltage stability.

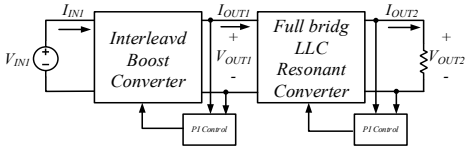


**FIGURE 35. Experimental serial architecture.**

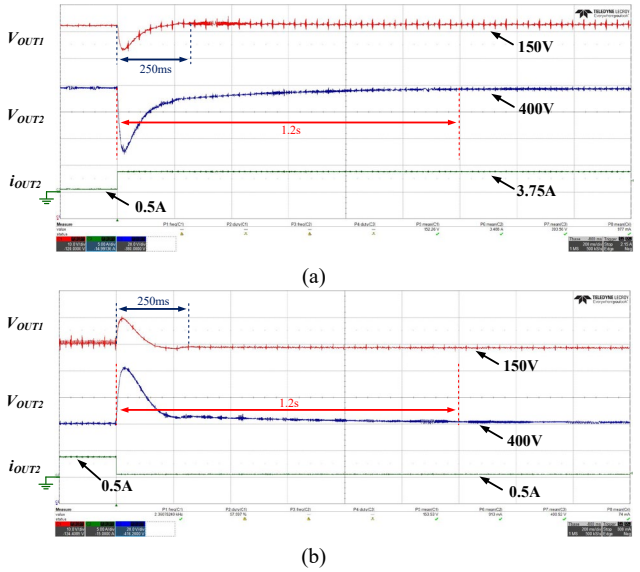


**FIGURE 36.** Waveform of load variation in low-voltage input mode((a) Raise load (b) Lower load).

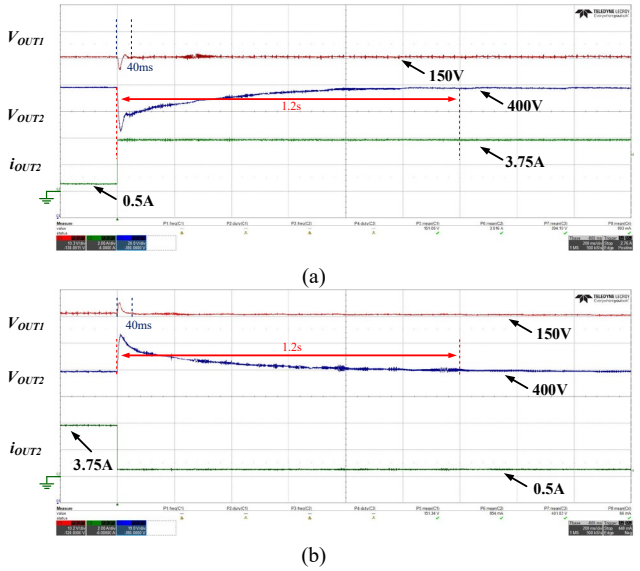


**FIGURE 37.** Waveform of load variation in high-voltage input mode ((a) Raise load (b) Lower load).

### *G. Efficiency Performance & Testing environment*

As shown in Fig. 38, the converter works in the low voltage input mode, the input voltage $V_{IN1}$ is 40V, and the efficiency curve of the constant voltage output under different load currents. The experimental results show that the highest efficiency of the low-voltage input mode is 92.69%.

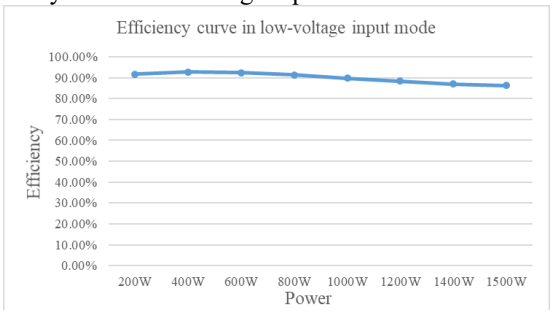


**FIGURE 38.** Efficiency curve in low-voltage input mode.

As shown in Fig. 39, the converter works in the high voltage input mode, the input voltage $V_{IN1}$ is 125V, and the efficiency curve under different load currents when the output voltage is constant. The experimental results show that the highest efficiency of the high-voltage input mode is 93.57%.

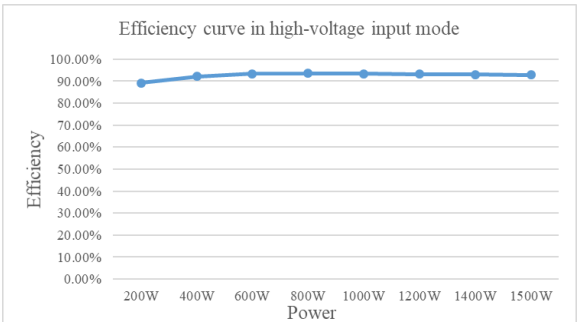


**FIGURE 39.** Efficiency curve in high-voltage input mode.

As shown in Fig. 40, the experimental test environment and setup of this converter.

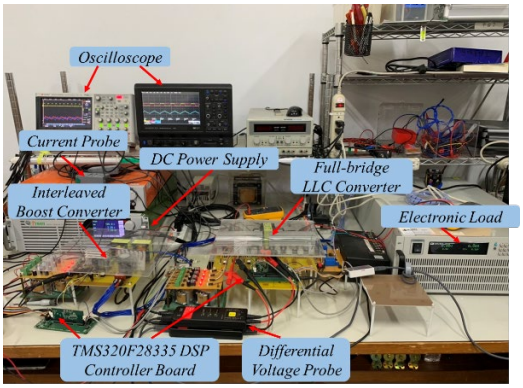


**FIGURE 40.** Testing environment and setup of the proposed converter.

## VI. Conclusion

This study presents and implements a high voltage conversion ratio interleaved boost series resonant converter. The proposed converter accommodates the wide input voltage characteristics of low-voltage fuel cells and meets the output voltage specifications of electric vehicle batteries. The converter employs an interleaved boost converter series with a full-bridge LLC resonant converter, which enhances the input current frequency through interleaving to reduce current ripple. Additionally, the full-bridge LLC resonant converter operates at an appropriate frequency, allowing for soft switching characteristics of both power switches and rectifying diodes, thereby improving overall converter efficiency. Ultimately, this research successfully achieved a power conversion of 1.5 kW from a wide input voltage range of 40–125 V to 400 V. Based on the experimental results, the conversion efficiency at low voltage input reached a maximum of 92.69%, while at high voltage input, the maximum efficiency attained was 93.57%. The experimental validation demonstrates that this converter can be applied to energy transfer systems for fuel cells with a wide input voltage range. Utilizing a DSP (Digital Signal Processor) as the system's core, the converter adjusts the output voltage

and signal processing control in response to load variations, thereby ensuring stable overall system output.

## References

[1] P. A. Lindahl, S. R. Shaw and S. B. Leeb, "Fuel Cell Stack Emulation for Cell and Hardware-in-the-Loop Testing," in IEEE Transactions on Instrumentation and Measurement, vol. 67, no. 9, pp. 2143-2152, Sept. 2018, doi: 10.1109/TIM.2018.2814070.

[2] L. Sun, G. Wu, Y. Xue, J. Shen, D. Li and K. Y. Lee, "Coordinated Control Strategies for Fuel Cell Power Plant in a Microgrid," in IEEE Transactions on Energy Conversion, vol. 33, no. 1, pp. 1-9, March 2018, doi: 10.1109/TEC.2017.2729881.

[3] A. Andreiciks, I. Steiks and O. Krievs, "Design of resonant DC/DC converter for fuel cell application," 2012 13th Biennial Baltic Electronics Conference, Tallinn, Estonia, 2012, pp. 219-222, doi: 10.1109/BEC.2012.6376856.

[4] B. M. Kumar, A. Kumar, A. H. Bhat and P. Agarwal, "Comparative study of dual active bridge isolated DC to DC converter with single phase shift and dual phase shift control techniques," 2017 Recent Developments in Control, Automation & Power Engineering (RDCAPE), Noida, India, 2017, pp. 453-458, doi: 10.1109/RDCAPE.2017.8358314.

[5] H. Bai and C. Mi, "Eliminate Reactive Power and Increase System Efficiency of Isolated Bidirectional Dual-Active-Bridge DC–DC Converters Using Novel Dual-Phase-Shift Control," in IEEE Transactions on Power Electronics, vol. 23, no. 6, pp. 2905-2914, Nov. 2008, doi: 10.1109/TPEL.2008.2005103.

[6] B. Zhao, Q. Yu and W. Sun, "Extended-Phase-Shift Control of Isolated Bidirectional DC–DC Converter for Power Distribution in Microgrid," in IEEE Transactions on Power Electronics, vol. 27, no. 11, pp. 4667-4680, Nov. 2012, doi: 10.1109/TPEL.2011.2180928.

[7] A. Kumar, A. H. Bhat and P. Agarwal, "Comparative analysis of dual active bridge isolated DC to DC converter with single phase shift and extended phase shift control techniques," 2017 6th International Conference on Computer Applications In Electrical Engineering-Recent Advances (CERA), Roorkee, India, 2017, pp. 397-402, doi: 10.1109/CERA.2017.8343363.

[8] B. Zhao, Q. Yu and W. Sun, "Bidirectional full-bridge DC-DC converters with dual phase-shifting control and its backflow power characteristic analysis", Proceedings of the CSEE, vol. 32, no. 12, pp. 43-50, 2012.

[9] Xintao Guo, Jiuchun Jiang, Liyong Niu, Jingxin Li and Yanqing Qu, "A 10kW DC-DC system based on a bidirectional high-frequency isolated dual active bridge DC-DC topology," 2011 IEEE Power Engineering and Automation Conference, Wuhan, China, 2011, pp. 50-54, doi: 10.1109/PEAM.2011.6134793.

[10] V. Jeyakarthikha and K. R. Vairamani, "Multiport bidirectional dc-dc converter for energy storage applications," 2014 International Conference on Circuits, Power and Computing Technologies [ICCPCT-2014], Nagercoil, India, 2014, pp. 411-417, doi: 10.1109/ICCPCT.2014.7054897.

[11] B. Zhao, Q. Song, W. Liu and Y. Sun, "Overview of Dual-Active-Bridge Isolated Bidirectional DC–DC Converter for High-Frequency-Link Power-Conversion System," in IEEE Transactions on Power Electronics, vol. 29, no. 8, pp. 4091-4106, Aug. 2014, doi: 10.1109/TPEL.2013.2289913.

[12] Po-Wa Lee, Yim-Shu Lee, D. K. W. Cheng and Xiu-Cheng Liu, "Steady-state analysis of an interleaved boost converter with coupled inductors," in IEEE Transactions on Industrial Electronics, vol. 47, no. 4, pp. 787-795, Aug. 2000, doi: 10.1109/41.857959.

[13] Bo Yang, F. C. Lee, A. J. Zhang and Guisong Huang, "LLC resonant converter for front end DC/DC conversion," APEC. Seventeenth Annual IEEE Applied Power Electronics Conference and Exposition (Cat. No.02CH37335), Dallas, TX, USA, 2002, pp. 1108-1112 vol.2, doi: 10.1109/APEC.2002.989382.

[14] Z. Li, J. Zhao, Z. Chen and G. Chen, "A Design Method for LCC Resonant Converter over Wide Load Range with Wide-range Input and Output," 2019 IEEE PES Asia-Pacific Power and Energy Engineering Conference (APPEEC), Macao, China, 2019, pp. 1-6, doi: 10.1109/APPEEC45492.2019.8994436.

[15] R. -L. Lin and C. -W. Lin, "Design criteria for resonant tank of LLC DC-DC resonant converter," IECON 2010 - 36th Annual Conference on IEEE Industrial Electronics Society, Glendale, AZ, USA, 2010, pp. 427-432, doi: 10.1109/IECON.2010.5674988.

[16] Bing Lu, Wenduo Liu, Yan Liang, F. C. Lee and J. D. van Wyk, "Optimal design methodology for LLC resonant converter," Twenty-First Annual IEEE Applied Power Electronics Conference and Exposition, 2006. APEC '06., Dallas, TX, USA, 2006, pp. 6 pp.-, doi: 10.1109/APEC.2006.1620590

[17] H. Wang and Z. Li, "A PWM LLC Type Resonant Converter Adapted to Wide Output Range in PEV Charging Applications," in IEEE Transactions on Power Electronics, vol. 33, no. 5, pp. 3791-3801, May 2018, doi: 10.1109/TPEL.2017.2713815.

[18] Y. Hu, J. Shao and T. S. Ong, "6.6 kW High-Frequency Full-Bridge LLC DC/DC Converter with SiC MOSFETs," 2019 IEEE Energy Conversion Congress and Exposition (ECCE), Baltimore, MD, USA, 2019, pp. 6848-6853, doi: 10.1109/ECCE.2019.8912805.

[19] S. -T. Wu and C. -H. Han, "Design and Implementation of a Full-Bridge LLC Converter With Wireless Power Transfer for Dual Mode Output Load," in IEEE Access, vol. 9, pp. 120392-120406, 2021, doi: 10.1109/ACCESS.2021.3107868.

[20] W. Na and H. Lee, "Sliding mode control design of current fed full bridge DC to DC converter for fuel cell applications," 2011 IEEE Power and Energy Conference at Illinois, 2011, pp. 1-4, doi: 10.1109/PECI.2011.5740491.

[21] M. S. K. Reddy and D. Elangovan, "Analysis and simulation of ZCS current-fed full bridge high gain DC-DC converter with Synchronous rectification," 2015 Conference on Power, Control, Communication and Computational Technologies for Sustainable Growth (PCCCTSG), 2015, pp. 183-187, doi: 10.1109/PCCCTSG.2015.7503902.

[22] C. Shi, H. Wang, S. Dusmez and A. Khaligh, "A SiC-Based High-Efficiency Isolated Onboard PEV Charger With Ultrawide DC-Link Voltage Range," in IEEE Transactions on Industry Applications, vol. 53, no. 1, pp. 501-511, Jan.-Feb. 2017, doi: 10.1109/TIA.2016.2605063.

[23] H. Wang, S. Dusmez and A. Khaligh, "Design and Analysis of a Full-Bridge LLC-Based PEV Charger Optimized for Wide Battery Voltage Range," in IEEE Transactions on Vehicular Technology, vol. 63, no. 4, pp. 1603-1613, May 2014, doi: 10.1109/TVT.2013.2288772.

[24] S. Sarani, H. Abootorabi Zarchi and H. Delavaripour, "Ripple-Free Input Current Flyback Converter Using a Simple Passive Circuit," in IEEE Transactions on Industrial Electronics, vol. 69, no. 3, pp. 2557-2564, March 2022, doi: 10.1109/TIE.2021.3065624.

[25] A. Gupta, N. Korada and R. Ayyanar, "Quadratic-Extended-Duty-Ratio Boost Converters for Ultra High Gain Application With Low Input Current Ripple and Low Device Stress," in IEEE Transactions on Industry Applications, vol. 59, no. 1, pp. 938-948, Jan.-Feb. 2023, doi: 10.1109/TIA.2022.3207132.

[26] H. Suryoatmojo et al., "Implementation of High Voltage Gain DC-DC Boost Converter for Fuel Cell Application," 2018 International Conference on Engineering, Applied Sciences, and Technology (ICEAST), Phuket, Thailand, 2018, pp. 1-4, doi: 10.1109/ICEAST.2018.8434428.

**Sen-Tung Wu** was born in Taipei, Taiwan, in 1980. He received the B.S., M.S., and Ph.D. degrees from the Department of Electronic and Computer Engineering, National Taiwan University of Science and Technology, Taiwan, in 2003, 2005, and 2014, respectively. He had working experience with the research and development department of switching power supply design manufacture for several years. In 2017, he was an assistant professor with the Department of Electrical Engineering, National Formosa University, Yunlin, Taiwan. He has been an associate professor with the EE Department, since 2022. His main research interests include power electronics, energy converter designs, battery chargers, bidirectional converters, power factor correction circuit design and wireless power transfer applications.

**Jun-Teng Hong** is from Changhua, Taiwan. He received the B.S. and M.S. degrees from the Department of Electrical Engineering, National Formosa University, Yunlin, in 2020 and 2022, respectively. He has been working with LITE-ON Technology Company, Taiwan, as an EE Research and Development Engineer, since 2023. His research interests include power electronics, wireless power transfer applications, bidirectional converter design. He is currently in charge of hybrid photovoltaic inverter project in LITE-ON.

**Ching-Chun Chuang** received the B.S. degree in electrical engineering from the National Kaohsiung University of Applied Sciences, Kaohsiung, Taiwan, in 2002. The M.S. degree in Electrical Engineering from Chun Yuan Christian University, Zhongli, Taiwan, in 2006. The Ph.D. degree in electronics engineering from the National Taiwan University of Science and Technology (NTUST), Taipei, Taiwan in 2013. He is currently an assistant professor with the National Kaohsiung University of Science and Technology, Kaohsiung, Taiwan. His research interests include high-power-density power converter, resonant converters, digitally controlled power electronics, and battery management systems.